HHS Public Access

Author manuscript

Cytometry A. Author manuscript; available in PMC 2020 May 09.

Published in final edited form as:

Cytometry A. 2020 May ; 97(5): 528–539. doi:10.1002/cyto.a.23872.

Single-Cell Intravital Microscopy of Trastuzumab Quantifies Heterogeneous *in vivo* Kinetics

Ran Li[1], **Adel Attari**[1], **Mark Prytyskach**[1], **Michelle A. Garlin**[1], **Ralph Weissleder**[1,2,3,#], **Miles A. Miller**[1,2,#]

[1]Center for Systems Biology, Massachusetts General Hospital, Boston, MA 02114.

[2]Department of Radiology, Massachusetts General Hospital and Harvard Medical School, Boston, MA 02114.

[3]Department of Systems Biology, Harvard Medical School, Boston, MA 02115.

Abstract

Cell-to-cell heterogeneity can substantially impact drug response, especially for monoclonal antibody (mAb) therapies that may exhibit variability in both delivery (pharmacokinetics) and action (pharmacodynamics) within solid tumors. However, it has traditionally been difficult to examine the kinetics of mAb delivery at a single-cell level and in a manner that enables controlled dissection of target-dependent and -independent behaviors. To address this issue, here we developed an in vivo confocal (intravital) microscopy approach to study single-cell mAb pharmacology in a mosaic xenograft comprising a mixture of cancer cells with variable expression of the receptor HER2. As a proof-of-principle, we applied this model to trastuzumab therapy, a HER2-targeted mAb widely used for treating breast and gastric cancer patients. Trastuzumab accumulated to a higher degree in HER2-over expressing tumor cells compared to HER2-low tumor cells (~5:1 ratio at 24 hrs after administration) but importantly, the majority actually accumulated in tumor-associated phagocytes. For example, 24 hours after IV administration over 50% of tumoral trastuzumab was found in phagocytes whereas at 48 hrs it was > 80%. Altogether, these results reveal the dynamics of how phagocytes influence mAb behavior *in vivo*, and demonstrate an application of intravital microscopy for quantitative single-cell measurement of mAb distribution and retention in tumors with heterogeneous target expression.

Keywords

tumor associated macrophage; metastatic breast cancer; human epidermal growth factor receptor 2 / HER2 / ERBB2; Fc-receptor; antibody-dependent cellular phagocytosis

Advances in single-cell profiling have made it clear that tumor tissue can be highly heterogenous (both within the cancer cell and also the host cell repertoire), and the dynamic clonal architecture of cancer plays a key role in disease progression and the emergence of

---

[#]Co-corresponding contact: rweissleder@mgh.harvard.edu, miles.miller@mgh.harvard.edu.

Conflicts of Interest:
The authors express no conflicts of interest but acknowledge provision of Tzm from the Genentech/Roche Outgoing Material Transfer Agreement (MTA) Program.

Author Manuscript

Author Manuscript

Author Manuscript

Author Manuscript

Author Manuscript

Author Manuscript

Author Manuscript

Author Manuscript

drug resistance (1). Cell-to-cell variability may be especially important in the context of drugs that specifically bind amplified or mutated targets, and past studies have shown how the expression of molecular drug targets can be lost as tumors evolve during treatment (2). The receptor tyrosine kinase erbB-2, also known as HER2, is a classic example of a drug target exhibiting this behavior: although *HER2/neu* amplification is observed in 15–30% of breast cancers (3) and 10–30% of gastric cancers (4), its expression level can be mixed across cancer cells in a given patient (5, 6), and reports have noted interconversion between HER2-positive and HER2-negative histological phenotypes following HER2-targeted therapy (7). Moreover, variation in the tumor microenvironment (TME) compounds intrinsic heterogeneity in cancer cells and their response to treatment. Mixed infiltrates of immune cells including cytotoxic T-cells and immunosuppressive tumor associated macrophages provide inflammatory or pro-survival signals to neighboring cancer cells (8), and directly participate in cytolytic (9) or phagocytic (10) cancer cell killing. Disordered tumor vascularization can cause hypoxia that impacts both immune and cancer cell behaviors (11), and leads to heterogeneous drug distribution within tumor tissues, especially for macromolecular therapies such as monoclonal antibodies (mAbs) that may inefficiently transport through tissue (12).

MAbs have been used as effective cancer treatments for decades, and benefit from specific and potent target binding, long circulating half-lives, and an ability to engage with the immune system to promote cell killing (9). The HER2-targeted trastuzumab (Tzm, marketed as Herceptin) (13, 14) is one of the oldest and most widely-used mAbs, and is FDA-approved for the treatment of HER2+ breast and gastric cancers (15). Unfortunately, primary and acquired resistances to Tzm and other HER2-targeted therapies are frequent in advanced disease, and many mAbs including Tzm exhibit dose-limiting systemic toxicities (16, 17). Thus, a clear need exists to understand mechanisms that govern the efficacy and selective delivery of mAbs, particularly in the context of HER2+ cancers.

One challenge in understanding the *in vivo* pharmacology of mAbs lies in the multi-component nature by which they function in the TME. Tumor-targeted mAbs typically act through a combination of cancer cell-intrinsic and -extrinsic effects that play out on cellular-level length scales (9). In the case of Tzm, cell-intrinsic effects include HER2 binding and subsequent inhibition of oncogenic kinase signaling (18), while cell-extrinsic effects include the Fc (fragment crystallizable region)-mediated roles that the immune system plays in response to mAb binding, such as antibody-dependent cell-mediated cytotoxicity (ADCC) (19) and antibody-dependent cellular phagocytosis (ADCP) (20). Cell-extrinsic effects have become even more relevant with the rise of mAb-drug conjugates, bi-specific mAbs, chimeric antigen receptor therapies, and immune checkpoint blockade. In the context of heterogeneous target expression, cell-extrinsic effects raise questions of how mAb binding and immune engagement in some cells can impact the behavior of others, for instance through bystander or abscopal effects. Collectively, the complexity in mAb pharmacology underscores the challenges optimizing mAb in a heterogenous TME — and motivate approaches to study mAb delivery and action *in vivo* at subcellular resolution.

To help address these questions, here we present a high-resolution intravital microscopy (IVM) platform to study the single-cell pharmacology of tumor-targeted mAb in a tumor

Author Manuscript Author Manuscript Author Manuscript Author Manuscript

with defined heterogeneity in target expression. As a proof of principle, we focus on Tzm since it is widely used clinically. New biologics and cell therapies have built upon Tzm in targeting HER2, and Tzm drug resistance continues to be a challenge (16, 21). As a model of intratumoral heterogeneity in HER2 expression (22, 23), we developed a mosaic xenograft model composed of a mixture of tumor cells with variable HER2 expression. We found that although Tzm binds efficiently and selectively on HER2+ cells, its accumulation was actually highest in tumor-associated phagocytes such as macrophages. On tumor cells, Tzm accumulation peaked after 24 h post-administration, while levels in neighboring phagocytes gradually increased for 2 days. Although HER2 over-expression on cancer cells was not required for a baseline accumulation of Tzm in tumor-associated phagocytes, it caused Tzm uptake by phagocytes to be ~3-fold enhanced on a per-cell basis. Altogether, these results provide a complementary perspective to recent studies examining the impact of tumor associated phagocytes on mAb biodistribution and action (24, 25), and demonstrate a proof-of-principle study of how IVM enables the tracking of mAbs through a heterogeneous tumor at a single-cell level. We anticipate this approach will be useful for studying the impact of mAbs on evolving intratumoral heterogeneity, and for investigating the roles macrophages and other immune cells play in promoting or blocking mAb action.

Materials and Methods

Cell Culture, transfection, and transduction.

SKBR3 and HCC1954 breast cancer cells were cultured in McCoy’s 5A modified media (Corning) or RPMI1640 media (Corning), respectively. MCF7 breast cancer cells, MDA-MB-231 breast cancer cells (MDA-231), and Raw 264.7 phagocytes, and HT-1080 fibrosarcoma cells (HT) were all cultured in Dulbecco’s modified eagle medium (Corning). All growth media were supplemented with 10% fetal bovine serum (Gibco), 100 IU penicillin, and 100 μg/mL streptomycin (Invitrogen). All cells were obtained from American Type Culture Collection (ATCC), cultured at 5% CO_2 and 37°C, and were routinely tested for mycoplasma contamination.

To generate HT cells expressing HER2 fused to GFP at the c-terminus (HT-HER2-GFP), parental HT cells were transfected with plasmid carrying HER2-GFP gene (Addgene plasmid # 39321, a gift from Dr. Martin Offterdinger) using Lipofectamine 3000 (Invitrogen) according to manufacturer protocols. Cells stably expressing HER2-GFP were clonally selected after initial 500 μg/ml geneticin selection for 7–10 days. HT-1080 cells expressing cytoplasmic BFP (HT-BFP) were generated by transducing wild-type HT-1080 cells with pLVX-BFP-IRES-PURO, and were subsequently selected with growth media containing 10 μg/ml of puromycin for 7 days. Cells with high expression of the fluorescent proteins were selected via fluorescence activated cell sorting (MGH Flow Cytometry Core). Despite clonal expansion in HT-HER2-GFP cells, heterogeneous expression emerged after serial passaging, which provided a range of HER2 expression to examine in subsequent experiments.

Author Manuscript Author Manuscript Author Manuscript Author Manuscript

Fluorescent Tzm labeling

Trastuzumab (Herceptin ®) was generously provided by Genentech via material transfer agreement, and was conjugated to AlexaFluor647 (A647) via N-Hydroxysuccinimide (NHS) -ester chemistry (Tzm-A647). Briefly, Tzm was dissolved in 0.1 M sodium bicarbonate at 10 mg/mL. AlexaFluor647 NHS ester (Thermo) was dissolved to 10 mg/mL in 0.5 mL anhydrous N,N-dimehtylformamide, which was then added to Tzm and stirred at room temperature for 1 h. 7K MWCO Zeba Spin Desalting Columns (Thermo) were used for purification following manufacturer guidelines. Molar ratio of fluorophore conjugation was determined by Nanodrop following manufacturer guidelines.

Flow cytometry

Flow cytometry analysis assessed the binding of Tzm to a panel of HER2-high and HER2-low cells, as well as the expression of HER2-GFP fusion protein in HT-HER2-GFP cells. Briefly, wash buffer was prepared as 3% fetal bovine serum (Gibco) in phosphate buffered saline (PBS, Corning) and kept on ice. All cells were trypsinized, washed, and incubated with 2 μg/mL of Tzm-A647 on ice for 90 minutes. Cells were again washed 3x and fixed with 1% paraformaldehyde (PFA) prior to analysis on a LSR II flow cytometer (BD Bioscience, equipped with 405, 488, and 633 nm lasers). Cells were included for analysis based on FSC-A x SSC-A gating criteria, while doublets were excluded from analysis based on FSC-A x FSC-H gating criteria. A647 and GFP signals from the cells were recorded and analyzed with FlowJo (Treestar).

Imaging of Tzm binding to HER2+ cells in vitro

Parental HT-1080, HT-BFP, HT-HER2-GFP, and SKBR3 cells were plated overnight at 50% confluency on 96-well plates (Ibidi). Tzm-A647 was incubated with the cells for 30 minutes at 5% CO_2 and 37 °C at 5 μg/mL. The cells were then washed 5 times with PBS, and fixed with 4% PFA (EMS). The cells were imaged with a DeltaVision (Applied Precision) modified BX63 microscope (Olympus) fitted with a camera (Andor).

Animal models and intravital microscopy

All animal research was carried out in compliance with guidelines from the Institutional Subcommittee on Research Animal Care (MGH). HT-BFP and HT-HER2-GFP mosaic xenograft tumors were established in dorsal skin-fold window chambers on female 6–12 weeks old nu/nu mice (Cox 7, MGH). Briefly, while mice were anesthetized with 2% isoflurane supplied with 2 L/min O_2, titanium window chambers (APJ Trading Co.) were surgically implanted on the back of the animals under sterile conditions. 10^6 HT-HER2-GFP and 10^6 HT-BFP cells were mixed and injected with 50 μL of PBS under the fascia layer of the skin inside the windows. Chambers were then sealed with sterile coverslips, and mice were prophylactically supplied with antibiotic in drinking water. Analgesic buprenorphine was administered before and for 3 days following surgery. Tumors grew for 2 weeks prior to imaging experiments. 24 h prior to imaging, AlexaFluor555 (A555)-labeled 500 kDa dextran (dex-A555) was administered to mice intravenously (i.v.) via tail-vein to label phagocytes including macrophages. On the day of the imaging experiment, the mice were anesthetized with isoflurane, tail-vein catheters were placed, and subjects were immobilized onto a heated

Author Manuscript Author Manuscript Author Manuscript Author Manuscript

microscope stage (37 °C) and monitored under anesthesia for the experiment duration. 200 μg of Tzm-A647 in 100 uL of PBS was administered by catheter, and time-lapse IVM was recorded with a FluoView FV1000 multi-photon confocal imaging system (Olympus) for 50 min. Separate imaging sessions were performed at 3 h, 24 h, and 48 h post-injection with Tzm, allowing for recovery from anesthesia and return to animal housing in between. Imaging the same low magnification field of view in repeated imaging sessions was achieved by a combination of cartesian positioning within the window chamber's defined structural features using a computer-guided stage, and identifying recognizable features in vascular and tumor shape. Low-magnification images of the tumor were taken with a XLFluor 2x air objective (NA=0.14, Olympus), while high-magnification images were recored with a XLUMPLFLN 20x water immersion objective (NA=1.0, Olympus). BFP, GFP, A555, and A647 were excited sequentially with 405 nm, 473 nm, 559 nm, and 635 nm diode lasers, respectively, in combination with DM405/473/559/635 nm dichroic beam splitters. The emitted light was separated with SDM473/560/640 nm beam splitters. BFP, GFP, A555, and A647 signals were then detected with BA430–455 nm, BA490–540 nm, BA575–620 nm, and BA655–755 nm emission filters (Olympus), respectively. For confocal imaging, images were collected at 10 μm interval in z-direction. Although an additional laser system is available for multiphoton imaging with the FV1000 microscope, here we solely used single-photon excitation with diode lasers. This improved the acquisition and post-processing workflow, particularly for time-lapse data, but restricted our imaging depth to within ~100 μm. In contrast, ex vivo imaging of optically cleared tissue was not restricted to the surface (see below). Single-fluorophore control experiments were performed with HT-BFP cells, HT-HER2-GFP cells, dex-A555 treated Raw 264.7 cells, and Tzm-A647 treated Raw 264.7 cells to ensure no bleed-through between imaging channels.

Optical clearing and ex-vivo tumor imaging

Xenografts were implanted on the back of the nu/nu mice without using window chambers. 10^6 HT-BFP were injected with 50 uL of PBS into one flank, while 10^6 HT-HER2-GFP were injected contralaterally. Tumors grew roughly 2 weeks until palpable, and A555-labeled 500 kDa dextran was i.v. injected 24 h prior to Tzm-A647 injection. 24 h post-administration with Tzm, mice were perfused with 20 mL of PBS followed by 10 mL of 4% PFA via cardiac puncture. Tumors were excised and further fixed in 4% PFA overnight, optically cleared with a modified CUBIC solution (26) for 2–3 days, and placed into a glass chamber for confocal imaging.

Image analysis

Images were analyzed with Fiji (NIH) and Matlab (MathWorks), and in some cases z-projections of the 3D image stacks were generated. Region of interests (ROIs) were produced by automatic thresholding and watershed segmentation. Cell segmentation was performed from 2D images in the x-y plane. ROIs were generated to define the boundaries of the tumor cells, phagocytes, or whole tumors for quantification. Specifically, cell borders of the phagocytes were estimated by automated thresholding of the Gaussian-blur filtered A555 channel using the RenyEntropy method, as described previously (27), and implemented here using Fiji. Segmented cells were then gated for dextran accumulation and size. For Tzm intensity quantification, the average fluorescence intensities (background

Author Manuscript Author Manuscript Author Manuscript Author Manuscript

subtracted, or percent increase over background for ease of comparison in Fig. 5B) were calculated for each ROI. The automated procedure yielded values that highly correlated with measurements of total cellular uptake attained by manual segmentation (Pearson correlation coefficient >0.95). For fluorescent line profile quantification (Fig. 6C), a straight line was drawn from outside of the tumor to the tumor core, and fluorescence intensities along such lines were quantified.

Statistical analysis

Throughout the manuscript, results were displayed as means +/− standard error of mean (s.e.m), and $\alpha = 0.05$ level of significance was used. Statistical analyses (two-tailed t test, ANOVA tests with Tukey post test, Spearman correlation test, and Pearson correlation test) were performed with GraphPad Prism 7.0.

Results

Development of a 4-channel intravital microscopy approach to monitor trastuzumab pharmacology

To study Tzm behavior in a tumor environment with heterogenous tumor cell populations, we designed an IVM approach based on mosaic xenografts containing cancer cells with mixed HER2 expression (Fig. 1a). Human HT1080 fibrosarcoma cancer cells were used as an endogenously HER2-negative model that has been extensively characterized by IVM in the dorsal window chamber mouse xenograft system (28, 29). These HER2-negative cells were stably labeled with blue fluorescent protein (mTagBFP; $\lambda_{ex} = 402$nm), hereafter referred to as HT-BFP. As matched HER2-positive cells, parental HT1080 were transfected to express a HER2-GFP fusion protein construct that had previously been employed in microscopy studies of HER2 subcellular trafficking (30). Stable HT-HER2-GFP transfectants were then mixed with HT-BFP cells and co-injected into mice to form tumors with heterogeneous HER2 expression from cell to cell. Tumor associated macrophages have been shown to play critical roles in the biodistribution of nanomedicines (29). In this work, we imaged tumor-associated phagocytic cells including macrophages with intravenously administered AlexaFluor555-labeled 500 kDa dextran (dex-A555). Fluorescently labeled dextrans have been widely used in intravital microscopy to label phagocytes including macrophages within the TME. Although 70 kDa dextran is commonly utilized in past literature, in this work we used 500 kDa dextran, which extravasates more slowly into tissue and therefore could be useful for more extended visualization of microvasculature upon administration. At 24 hr post-injection, both 70 kDa and 500 kDa dextran are known to accumulate in phagocytes, and both have been used in past reports for macrophage imaging (27, 31). Tzm was labeled with AlexaFluor647 (λex=650 nm) via N-Hydroxysuccinimide (NHS)-ester conjugation (Fig. 1b), with a 6:1 (molecule of dye:molecule of mAb) degree of labeling, following previous guidelines (32). Overall, this 4-channel (BFP/GFP/A555/A647) setup enables the comparison of Tzm uptake by HER2+ and HER2− tumor cells and phagocytes in a matched TME. Each of the 4 fluorescence channels were imaged sequentially using unique excitation and emission filters (Fig. 1a), thus yielding minimal fluorescence bleed-through between channels as determined through single-color controls (Supplementary Fig. 1). Importantly, the mosaic imaging approach mitigates confounding

Author Manuscript Author Manuscript Author Manuscript Author Manuscript

variable effects, such as differences in vascularization or extracellular matrix content, that might occur when comparing behavior across separate HER2− and HER2+ tumors. In addition, the mosaic tumor model may also be somewhat representative of intratumoral heterogeneity that is found in patients, for instance as has been noted in HER2-expressing breast and especially gastric cancers (6, 33) (Fig. 1c).

We first performed *in vitro* studies to characterize the 4-channel imaging approach. To confirm that A647-labeled Tzm (Tzm-A647) exhibited sufficient fluorescence and efficient HER2 binding affinity, we treated a panel of cells expressing high HER2 (HCC1954 and SKBR3) or low HER2 (MCF7, MDA231, and parental HT1080) with Tzm. Flow cytometry analysis showed Tzm bound at 70 ± 40 fold higher levels (± s.d.) to cells with high HER2 (SKBR3 and HCC1954) compared to cells with low HER2 (MCF7, MDA231, and parental HT1080; Fig. 2a). Consistent with these data, past reports indicate that SKBR3 express $>10^6$ HER2 receptors per cell, while MCF7 express ~20-fold less (34). In another example, MDA231 were previously reported as having 40,000 HER2 receptors per cell while SKBR3 had approximately 30-fold higher (1.2×10^6) (35), and in the present study we found Tzm binding to be roughly 50-fold higher in SKBR3 compared to MDA231 (Fig. 2a). Importantly, the parental HT1080 cells show even lower Tzm binding than the MCF7 and MDA231 breast cancer cells, which are traditionally classified as HER2-negative. As expected, HT-BFP and parental HT1080 cells bound similarly low levels of Tzm (Fig. 2a). In contrast, HT-HER2-GFP cells exhibited Tzm binding comparable to other HER2-high breast cancer cell lines (HCC1954 and SKBR3). More precise interpretation of fold-change Tzm accumulation across cell lines would need to account for possible cell line heterogeneity among prior studies and would employ additional controls for absolute quantification, such as with synthetic bead standards (36). More importantly, HER2-GFP and Tzm signals on HT-HER2-GFP cells co-localized on a pixel-by-pixel basis, as seen by fluorescence microscopy (Fig. 2b–c, Supplementary Fig. 2). Taken together, these results demonstrate that Tzm selectively binds HER2-GFP fusion protein in the HT1080 model, and that HT-HER2-GFP approximates HER2+ breast cancer cells in their level of HER2 expression and Tzm binding.

To examine the ability to accurately distinguish HT-BFP and HT-HER2-GFP cells *in vivo*, we mixed the cells 1:1 and injected them into the dorsal window chamber of nu/nu mice. Upon tumor formation ~2 weeks later, IVM confirmed the establishment of mosaic tumors containing both BFP+ and GFP+ cells intermingled with each other (Fig. 3a). At a single cell (Fig. 3a) and pixel-by-pixel level (Fig. 3b), no substantial overlap of BFP and GFP signals was observed, indicating HER2+ and HER2− cells can be accurately distinguished from each other.

Systemic pharmacokinetics and single-cell accumulation using time-lapse IVM

We used time-lapse IVM to evaluate the first step of Tzm drug delivery to tumor: the extravasation of Tzm from blood vessels into the tumor interstitium. Within 10 minutes of i.v. injection, Tzm reached the tumor microvasculature surrounded by a mixture of HT-HER2-GFP and HT-BFP tumor cells (Fig. 4a). Over the course of 24 h, Tzm began extravasating from microvasculature into the interstitial space occupied by tumor cells, as

Author Manuscript Author Manuscript Author Manuscript Author Manuscript

evident by the decreasing Tzm signal intensity in the vessels and a corresponding increase in intensity outside of the vessels (Fig. 4a–d). Quantification of intravascular Tzm revealed an initial (or distribution-phase) blood half-life of roughly 40 min and terminal (or elimination-phase) blood half-life of 1.6 days according to a two-phase-exponential decay model (Fig. 4c), which is similar to previously reported values for an anti-PD1 mAb in a mouse xenograft model (24). 3 h post injection, a significant portion of Tzm had entered tumoral space, especially near tumor vasculature, and limited penetration into poorly vascularized tumor regions was noted (Fig. 4b,d). By 24 h, intratumoral Tzm signals were decreased compared to what was observed at 3 h inside the tumor, presumably due to the clearance of unbound drug. Tzm was hardly detectable in the tumor blood vessels at 24 h post injection compared to levels seen in tissue (Fig. 4b–d).

Complementary high-magnification IVM allowed us to quantify Tzm biodistribution within the tumor at a single-cell level. Tumor-associated phagocytes including macrophages were visualized with dex-A555, which was injected 24 h prior to Tzm administration. Images were then acquired at 3 h, 24 h, and 48 h post-injection of Tzm. BFP, GFP, or A555 fluorescence signals were observed to be individually high in HT-BFP, HT-HER2-GFP, or dex-A555+ cells, respectively, indicating minimal bleed-through among all three fluorescence channels *in vivo* and an ability to accurately distinguish cell-types from each other (Supplementary Fig. 3). In contrast to the strong co-localization observed between HER2-GFP and Tzm found *in vitro* (Fig. 2b), IVM revealed more modest Tzm accumulation in HT-HER2-GFP cells *in vivo* (Fig. 5a). Instead, a notably high degree of co-localization was seen between dex-A555+ phagocytes and Tzm at all time points (Fig. 5a, Supplementary Fig. 3). To quantify drug uptake at single cell level, fluorescent signals from each cell-type were segmented to delineate the boundary of these cells (Fig. 5a), and Tzm fluorescence was quantified on a cell-by-cell basis (Fig. 5b). As expected, Tzm uptake in HT-BFP cells was minimal, amounting to a range of only 20–80% increase in signal intensity above the auto-fluorescent background across the three time points. In contrast, Tzm signals in phagocytes were on average 400–950% above the background, as a range across the three time points. Phagocytes showed 470% increase in average Tzm uptake compared to HT-BFP tumor cells at 3 h, and 4000% increase in average uptake at 48 h. Phagocyte uptake of Tzm was also heterogenous, such that some dex-A555+ cells accumulated less Tzm than HT-BFP tumor cells, while others accumulated >30-fold more.

Although HT-HER2-GFP cells accumulated less Tzm than phagocytes, the average levels of Tzm associated with HT-HER2-GFP cells ranged from 100–600% more than that of HT-BFP cells across all time points (Fig. 5b). Moreover, Tzm uptake in HT-HER2-GFP cells substantially correlated with HER2-GFP fusion protein expression on a cell-by-cell level at 3 h and 24 h after Tzm administration (Fig. 5c), suggesting specific binding of Tzm to its targets. As a negative control, Tzm uptake by HT-BFP cells in the same mosaic tumor was quantified, and no correlation between Tzm uptake and BFP signal intensity was detected (Supplementary Fig. 4). This control thus suggests that the correlation between Tzm and HER2-GFP is not likely to have arisen from confounding factors such as tumor hypoxia/necrosis, which might have explained both inefficient fluorescent protein expression and poor drug delivery.

Author Manuscript

Author Manuscript

Author Manuscript

Author Manuscript

While Tzm bound selectively to HER2+ tumor cells in a manner that quantitatively correlated with HER2 expression and peaked at 24 h, accumulation was nonetheless highest in tumor-associated phagocytes (Fig. 5d). The change in Tzm distribution from 24 h to 48 h post-injection suggests that phagocytes actively accumulated an increasing fraction of Tzm in the tumor. In this late time frame, tumor-cell associated Tzm decreased, while phagocyte uptake continued to increase. Moreover, the cell-by-cell correlation between HER2-GFP expression and Tzm accumulation decreased by 70% from 24 h to 48 h (Fig. 5c). Indeed, at 24 h, the top 20% highest HER2-expressing tumor cells all had moderate Tzm accumulation (20th percentile or higher), while only 54% did by 48 h (Supplementary Fig. 5). This suggests that Tzm on HER2+ cells was removed or degraded by 48 h.

We also used IVM to quantify the relative abundance of tumor cells and phagocytes in the mosaic tumor (Fig. 5e). Although phagocytes were less abundant than tumor cells, they contributed to ~50% of total Tzm accumulation in the tumor at the first 24 h due to their high Tzm uptake on a per-cell basis (Fig. 5f). By 48 h, phagocytes accounted for 82 ± 19% of total Tzm accumulation in the tumor. This trend is explained by both an increase in phagocyte uptake and a decrease in Tzm association with tumor cells on a per-cell basis, as the cellular composition of the tumor did not change as substantially over the course of 48 h (Fig. 5e and Supplementary Table 1). In sum, these data suggest that phagocytes are the main reservoir for tumoral Tzm in this model, especially at late time -points following Tzm administration.

HER2 expression in tumor cells enhances phagocyte uptake of Tzm

We next investigated whether HER2 expression on tumor cells was required for phagocyte uptake of Tzm in tumor. To answer this question in a controlled manner, we established a xenograft model in which HT-BFP were injected in one flank, and HT-HER2-GFP were contralaterally injected (Fig. 6a). Unlike the mosaic tumor model, the contralaterally implanted HT-BFP and HT-HER2-GFP tumors exhibited relatively homogenous low or high HER2 expression, respectively. Tzm was injected intravenously following tumor formation, and the tumors were then excised 24 h later, optically cleared with CUBIC solution (26), and confocally imaged. Phagocyte uptake of Tzm was detectable in both type of tumors. However, Tzm uptake in the HT-HER2-GFP tumors was 3.6-fold (or 260% increase) that of the HT-BFP tumors (Fig. 6b–d). Most Tzm accumulated at the tumor periphery for both tumor types (Fig. 6c and Supplementary Fig. 6), where phagocytes including tumor-associated macrophages are known to reside at high levels, especially in the HT1080 model used here (31, 37, 38). Indeed, high-magnification images showed that most Tzm accumulated within phagocytes rather than tumor cells, regardless of HER2 expression (Fig. 6e). Although the amount of phagocytes in either tumor type was not significantly different (Fig. 6f), the phagocyte uptake of Tzm in HT-HER2-GFP tumors, on a per-cell basis, was 3.8-fold that of the HT-BFP tumors (Fig. 6g). Importantly, phagocyte uptake of dex-A555 showed no such difference (Supplementary Fig. 7), indicating enhanced Tzm uptake by phagocytes in HER2+ tumors was not due to underlying differences in general phagocytic capacity or tumor vasculatures. These results demonstrate that even though HER2 expression is not required for phagocyte uptake of Tzm in tumor, it can nonetheless lead to a higher tumoral mAb accumulation.

Author Manuscript Author Manuscript Author Manuscript Author Manuscript

Discussion

This study presents an IVM-based approach to simultaneously track i) the pharmacokinetics and selective association of mAb with its putative targets in tumors, ii) heterogeneous target expression on cancer cells, and iii) infiltrating immune populations, all at the single-cell level. This work builds on the growing development of IVM as a tool for studying drug pharmacology in cancer, and previous reports have used IVM to examine the behavior of cytotoxic chemotherapies (28, 39–44), targeted kinase (45–48) and poly-ADP ribose polymerase (44, 49) inhibitors, nanoparticle-encapsulated therapeutics (29, 50–54), and anti-PD1 immune checkpoint blockade mAb therapy (24, 26, 27). In several cases, mosaic xenograft models have been successfully used to test the impact of a particular protein on drug pharmacology, while holding other features of the TME relatively constant. For instance, IVM visualized the difference in drug accumulation and resistance caused by multi-drug resistance mutation 1 (MDR1) over-expression, and the mosaic strategy allowed intracellular drug levels to be compared between MDR1-positive and adjacent MDR1-negative cells in the same tumor region (28). In the present work, we extended the mosaic xenograft IVM strategy to study tumor-targeted mAbs, using HER2-targeted Tzm as a proof of principle model. Although Tzm has been studied and clinically used for decades, the contributions of tumor heterogeneity and immune uptake to its activity continue to be extensively studied. HER2-targeting remains highly relevant with next-generation immunotherapies, the clinical need remains great as patients frequently develop resistance, and over 300 Tzm clinical trials are currently registered as ongoing or recruiting. As an initial demonstration, we relied on a well-characterized and experimentally robust model based on the subcutaneous implantation of HT1080 cells, which has the advantage of using the dorsal window chamber for stable time-lapse imaging. In the present application, this model also has the advantage of lacking substantial levels of endogenous HER2 expression, such that the majority of HER2 expression in the TME is directly quantifiable through its fusion GFP reporter. Nonetheless, IVM setups have already been developed and applied for imaging cancer cell metastasis in orthotopic and autochthonous models of breast cancer, including with the use of a mammary fat pad window chamber and with *HER2/neu* driven genetically engineered mouse models (55). Such models may be especially valuable for studying drug distribution in a fully competent immune system and TME features specific to the mammary fat pad, but may face trade-offs in terms of imaging resolution, stability, restriction to mAbs targeting rodent instead of human antigen, and investment of resources.

Single-photon excitation was used in our intravital experiments. No signs of phototoxicity, as assessed by changes in cell morphology or blebbing, were observed in the present study or in prior reports that used similar imaging parameters (27). However, it is possible that more frequent imaging at higher power density could be phototoxic, potentially influencing HER2 expression in cancer cells and phagocytic activity in immune cells. Multiphoton microscopy may be especially appropriate in this case, since it is known to be less phototoxic than single-photon approaches in some applications (56). Moreover, in the present study, images were collected at 10 μm intervals in z-direction, and cell segmentation was performed from 2D images in the x-y plane. Higher z-axis resolution is technically feasible and has been successfully used in the past to support 3D segmentation (53, 57).

Author Manuscript Author Manuscript Author Manuscript Author Manuscript

Such increased resolution may potentially improve quantification of Tzm uptake but comes with the trade-off of added time for image acquisition, which can impact spatial coverage of the TME and create a greater potential for photobleaching.

We found that even though cellular uptake of Tzm can be highly heterogenous, Tzm still clearly associated with HER2+ tumor cells to a degree that correlated with the amount of HER2 expression. Despite this demonstrated specificity in mAb targeting, we nevertheless found that tumor-associated phagocytes accumulated even more Tzm than the highest-expressing HER2+ tumor cells, and roughly 80% of Tzm was phagocyte-associated by 48 h post-administration. Controlled experiments on matched tumors expressing or lacking HER2 showed that phagocytes in HER2+ tumors accumulated ~280% more Tzm than those in HER2− tumors, even though Tzm uptake by phagocyte was detectable in both. All in all, these results suggest both HER2 dependent and independent pathways of Tzm uptake by phagocytes, and previous experiments have confirmed that such dextran-accumulating phagocytes are primarily macrophages (58).

In principle, substantial differences in vascularization, vascular permeability, interstitial fluid pressure, and other microenvironment features could contribute to mechanisms of enhanced Tzm accumulation in HER2+ compared to HER2− tumors that don’t actually depend on HER2-Tzm binding. As with mAbs, high molecular-weight 500 kDa dextran transport into tumor tissue can be limited by tumor perfusion and extravasation out of vessels, and we hypothesized that differences in vascularization between HER2+ and HER2− tumors would also lead to differential dextran accumulation. However, no such difference was observed, therefore suggesting both tumors enabled comparable degrees of macromolecular accumulation (Supplementary Fig. 7). Additional control studies may be performed to more thoroughly characterize potential differences in the microanatomical structure of HER2+ and HER2− tumors that extend beyond the present report, and additional non-HER2 targeting compounds could also be compared, such as non-targeted mAbs. Further, it is possible to evaluate HER2-dependent Tzm uptake by phagocytes with *in vivo* competition experiments using no-fluorescent Tzm. However, we note that such competition experiment could be complicated to interpret, as prior reports have counter-intuitively found that co-administration of multiple types of HER2-targeted mAbs can lead to enhanced tumor penetration, for instance by mitigating the impact of the binding site barrier (59).

Is phagocyte uptake of mAbs beneficial for efficacy? Based on prior studies, HER2-independent phagocyte uptake may involve scavenging of interstitial Tzm, for instance via nonspecific macropinocytosis or Fc-mediated uptake of unbound mAbs by macrophages (60–62). In contrast, HER2-dependent enhancement in phagocyte uptake likely involves the interaction between HER2-bound Tzm and highly-expressed Fcγ receptors (FcγR) on phagocytes. Chimeric mAbs with humanized Fc domain (63), such as Tzm and rituximab, engage with murine FcγR, and pro-inflammatory FcγRIII contributes to their efficacy (19, 64). Activating FcγR on immune cells can engage tumor-bound mAbs and trigger ADCP and ADCC. Moreover, in the context of antibody drug conjugates (ADCs), Fc-mediated ADC uptake by tumor associated macrophages can contribute to ADC efficacy, even for non-targeted IgG ADCs (65). This latter result bears similarity to findings seen with drug-loaded nanoparticles, which also can accumulate in tumor associated macrophages. IVM has

Author Manuscript
Author Manuscript
Author Manuscript
Author Manuscript

visualized drug payload in these nanoparticles as slowly leaching out of the macrophages and transferring to surrounding cancer cells (29). In contrast, another IVM study found that Fc-mediated macrophage uptake of mAbs could actually be detrimental to efficacy by sequestering mAbs and preventing them from acting on their target: PD1-targeted mAbs that were bound to CD8+ T cells could be stripped and transferred to macrophages. mAb transfer did not involve ADCP, but instead depended on Fcglycosylation (24). These data collectively show important if complicated roles for macrophages, and time-lapse IVM has proven to be a powerful tool for dissecting them. Hence, further studies are still needed to clarify what determines the balance of beneficial vs. detrimental mAb uptake by phagocytes. Key factors may involve biased engagement with activating and inhibiting FcγRs, and myeloid phenotypes along the spectrum of M1 to M2 polarization.

We envision that the experimental strategy presented here can be extended to the pharmacokinetic study of other tumor- and immune-targeted mAbs, bi-specifics, ADCs, and even CAR-T or CAR-phagocytic cells (66). We demonstrated the utilities of this approach by uncovering the dynamics of Tzm accumulation in heterogeneous tumor cells and especially in tumor-associated phagocytes, therefore highlighting a potential value in monitoring and manipulating the TME and phagocyte content of tumors to improve therapeutic outcomes. Since phagocyte uptake can be mediated by FcγR, our results help provide context to the observation that FcγR polymorphisms correlate with patient responses to Tzm treatment (67), and motivate Fc-domain engineering (24). Importantly, the IVM approach developed in this study could be used to evaluate the efficacy of such new treatment strategies.

Supplementary Material

Refer to Web version on PubMed Central for supplementary material.

Acknowledgments:

This work was supported in parts by NIH/NCI grants U01CA206997, T32CA079443, R00CA207744, and an ATA ThyCa Research Grant.

Literature Cited:

1. Dagogo-Jack I, and Shaw AT. 2018 Tumour heterogeneity and resistance to cancer therapies. Nat Rev Clin Oncol 15: 81–94. [PubMed: 29115304]
2. McGranahan N, and Swanton C. 2017 Clonal Heterogeneity and Tumor Evolution: Past, Present, and the Future. Cell 168: 613–628. [PubMed: 28187284]
3. Burstein HJ 2005 The distinctive nature of HER2-positive breast cancers. N Engl J Med 353: 1652–1654. [PubMed: 16236735]
4. Gravalos C, and Jimeno A. 2008 HER2 in gastric cancer: a new prognostic factor and a novel therapeutic target. Ann Oncol 19: 1523–1529. [PubMed: 18441328]
5. Buckley NE, Forde C, McArt DG, Boyle DP, Mullan PB, James JA, Maxwell P, McQuaid S, and Salto-Tellez M. 2016 Quantification of HER2 heterogeneity in breast cancer-implications for identification of sub-dominant clones for personalised treatment. Sci Rep 6: 23383. [PubMed: 26996207]
6. Lee HJ, Seo AN, Kim EJ, Jang MH, Suh KJ, Ryu HS, Kim YJ, Kim JH, Im SA, Gong G, Jung KH, Park IA, and Park SY. 2014 HER2 heterogeneity affects trastuzumab responses and survival in

Author Manuscript

Author Manuscript

Author Manuscript

Author Manuscript

patients with HER2-positive metastatic breast cancer. Am J Clin Pathol 142: 755–766. [PubMed: 25389328]

7. Jordan NV, Bardia A, Wittner BS, Benes C, Ligorio M, Zheng Y, Yu M, Sundaresan TK, Licausi JA, Desai R, O'Keefe RM, Ebright RY, Boukhali M, Sil S, Onozato ML, Iafrate AJ, Kapur R, Sgroi D, Ting DT, Toner M, Ramaswamy S, Haas W, Maheswaran S, and Haber DA. 2016 HER2 expression identifies dynamic functional states within circulating breast cancer cells. Nature 537: 102–106. [PubMed: 27556950]
8. Quail DF, and Joyce JA. 2013 Microenvironmental regulation of tumor progression and metastasis. Nat Med 19: 1423–1437. [PubMed: 24202395]
9. Scott AM, Wolchok JD, and Old LJ. 2012 Antibody therapy of cancer. Nat Rev Cancer 12: 278–287. [PubMed: 22437872]
10. Weiskopf K, and Weissman IL. 2015 Macrophages are critical effectors of antibody therapies for cancer. MAbs 7: 303–310. [PubMed: 25667985]
11. Petrova V, Annicchiarico-Petruzzelli M, Melino G, and Amelio I. 2018 The hypoxic tumour microenvironment. Oncogenesis 7: 10. [PubMed: 29362402]
12. Stylianopoulos T, Munn LL, and Jain RK. 2018 Reengineering the Tumor Vasculature: Improving Drug Delivery and Efficacy. Trends Cancer 4: 258–259. [PubMed: 29606306]
13. Carter P, Presta L, Gorman CM, Ridgway JB, Henner D, Wong WL, Rowland AM, Kotts C, Carver ME, and Shepard HM. 1992 Humanization of an anti-p185HER2 antibody for human cancer therapy. Proc Natl Acad Sci U S A 89: 4285–4289. [PubMed: 1350088]
14. Fendly BM, Winget M, Hudziak RM, Lipari MT, Napier MA, and Ullrich A. 1990 Characterization of murine monoclonal antibodies reactive to either the human epidermal growth factor receptor or HER2/neu gene product. Cancer Res 50: 1550–1558. [PubMed: 1689212]
15. Arteaga CL, Sliwkowski MX, Osborne CK, Perez EA, Puglisi F, and Gianni L. 2011 Treatment of HER2-positive breast cancer: current status and future perspectives. Nat Rev Clin Oncol 9: 16–32. [PubMed: 22124364]
16. Nahta R, and Esteva FJ. 2007 Trastuzumab: triumphs and tribulations. Oncogene 26: 3637–3643. [PubMed: 17530017]
17. Pohlmann PR, Mayer IA, and Mernaugh R. 2009 Resistance to Trastuzumab in Breast Cancer. Clin Cancer Res 15: 7479–7491. [PubMed: 20008848]
18. Nahta R, and Esteva FJ. 2006 Herceptin: mechanisms of action and resistance. Cancer Lett 232: 123–138. [PubMed: 16458110]
19. Clynes RA, Towers TL, Presta LG, and Ravetch JV. 2000 Inhibitory Fc receptors modulate in vivo cytotoxicity against tumor targets. Nat Med 6: 443–446. [PubMed: 10742152]
20. Shi Y, Fan X, Deng H, Brezski RJ, Rycyzyn M, Jordan RE, Strohl WR, Zou Q, Zhang N, and An Z. 2015 Trastuzumab triggers phagocytic killing of high HER2 cancer cells in vitro and in vivo by interaction with Fcγ receptors on macrophages. J Immunol 194: 4379–4386. [PubMed: 25795760]
21. Iwata TN, Ishii C, Ishida S, Ogitani Y, Wada T, and Agatsuma T. 2018 A HER2-Targeting Antibody-Drug Conjugate, Trastuzumab Deruxtecan (DS-8201a), Enhances Antitumor Immunity in a Mouse Model. Mol Cancer Ther 17: 1494–1503. [PubMed: 29703841]
22. Seol H, Lee HJ, Choi Y, Lee HE, Kim YJ, Kim JH, Kang E, Kim SW, and Park SY. 2012 Intratumoral heterogeneity of HER2 gene amplification in breast cancer: its clinicopathological significance. Mod Pathol 25: 938–948. [PubMed: 22388760]
23. Szöllösi J, Balázs M, Feuerstein BG, Benz CC, and Waldman FM. 1995 ERBB-2 (HER2/neu) gene copy number, p185HER-2 overexpression, and intratumor heterogeneity in human breast cancer. Cancer Res 55: 5400–5407. [PubMed: 7585609]
24. Arlauckas SP, Garris CS, Kohler RH, Kitaoka M, Cuccarese MF, Yang KS, Miller MA, Carlson JC, Freeman GJ, Anthony RM, Weissleder R, and Pittet MJ. 2017 In vivo imaging reveals a tumor-associated macrophage-mediated resistance pathway in anti-PD-1 therapy. Sci Transl Med 9:
25. Gordon SR, Maute RL, Dulken BW, Hutter G, George BM, McCracken MN, Gupta R, Tsai JM, Sinha R, Corey D, Ring AM, Connolly AJ, and Weissman IL. 2017 PD-1 expression by tumour-associated macrophages inhibits phagocytosis and tumour immunity. Nature 545: 495–499. [PubMed: 28514441]

Author Manuscript Author Manuscript Author Manuscript Author Manuscript

26. Cuccarese MF, Dubach JM, Pfirschke C, Engblom C, Garris C, Miller MA, Pittet MJ, and Weissleder R. 2017 Heterogeneity of macrophage infiltration and therapeutic response in lung carcinoma revealed by 3D organ imaging. Nat Commun 8: 14293. [PubMed: 28176769]
27. Rodell CB, Arlauckas SP, Cuccarese MF, Garris CS, Li R, Ahmed MS, Kohler RH, Pittet MJ, and Weissleder R. 2018 TLR7/8-agonist-loaded nanoparticles promote the polarization of tumour-associated macrophages to enhance cancer immunotherapy. Nat Biomed Eng 2: 578–588.
28. Laughney AM, Kim E, Sprachman MM, Miller MA, Kohler RH, Yang KS, Orth JD, Mitchison TJ, and Weissleder R. 2014 Single-cell pharmacokinetic imaging reveals a therapeutic strategy to overcome drug resistance to the microtubule inhibitor eribulin. Sci Transl Med 6: 261ra152.
29. Miller MA, Zheng YR, Gadde S, Pfirschke C, Zope H, Engblom C, Kohler RH, Iwamoto Y, Yang KS, Askevold B, Kolishetti N, Pittet M, Lippard SJ, Farokhzad OC, and Weissleder R. 2015 Tumour-associated macrophages act as a slow-release reservoir of nano-therapeutic Pt(IV) pro-drug. Nat Commun 6: 8692. [PubMed: 26503691]
30. Offterdinger M, and Bastiaens PI. 2008 Prolonged EGFR signaling by ERBB2-mediated sequestration at the plasma membrane. Traffic 9: 147–155. [PubMed: 17956594]
31. Wyckoff JB, Wang Y, Lin EY, Li JF, Goswami S, Stanley ER, Segall JE, Pollard JW, and Condeelis J. 2007 Direct visualization of macrophage-assisted tumor cell intravasation in mammary tumors. Cancer Res 67: 2649–2656. [PubMed: 17363585]
32. Nanda JS, and Lorsch JR. 2014 Labeling a protein with fluorophores using NHS ester derivitization. Methods Enzymol 536: 87–94. [PubMed: 24423269]
33. Lee HE, Park KU, Yoo SB, Nam SK, Park DJ, Kim HH, and Lee HS. 2013 Clinical significance of intratumoral HER2 heterogeneity in gastric cancer. Eur J Cancer 49: 1448–1457. [PubMed: 23146959]
34. Hendriks BS, Klinz SG, Reynolds JG, Espelin CW, Gaddy DF, and Wickham TJ. 2013 Impact of tumor HER2/ERBB2 expression level on HER2-targeted liposomal doxorubicin-mediated drug delivery: multiple low-affinity interactions lead to a threshold effect. Mol Cancer Ther 12: 1816–1828. [PubMed: 23723124]
35. Costantini DL, Bateman K, McLarty K, Vallis KA, and Reilly RM. 2008 Trastuzumab-resistant breast cancer cells remain sensitive to the auger electron-emitting radiotherapeutic agent 111In-NLS-trastuzumab and are radiosensitized by methotrexate. J Nucl Med 49: 1498–1505. [PubMed: 18703606]
36. Miller MA, Moss ML, Powell G, Petrovich R, Edwards L, Meyer AS, Griffith LG, and Lauffenburger DA. 2015 Targeting autocrine HB-EGF signaling with specific ADAM12 inhibition using recombinant ADAM12 prodomain. Sci Rep 5: 15150. [PubMed: 26477568]
37. Kim HY, Li R, Ng TSC, Courties G, Rodell CB, Prytyskach M, Kohler RH, Pittet MJ, Nahrendorf M, Weissleder R, and Miller MA. 2018 Quantitative Imaging of Tumor-Associated Macrophages and Their Response to Therapy Using 64Cu-Labeled Macrin. ACS Nano 12: 12015–12029. [PubMed: 30508377]
38. Ohno S, Ohno Y, Suzuki N, Kamei T, Koike K, Inagawa H, Kohchi C, Soma G, and Inoue M. 2004 Correlation of histological localization of tumor-associated macrophages with clinicopathological features in endometrial cancer. Anticancer Res 24: 3335–3342. [PubMed: 15515429]
39. Arvanitis CD, Askoxylakis V, Guo Y, Datta M, Kloepper J, Ferraro GB, Bernabeu MO, Fukumura D, McDannold N, and Jain RK. 2018 Mechanisms of enhanced drug delivery in brain metastases with focused ultrasound-induced blood-tumor barrier disruption. Proc Natl Acad Sci U S A 115: E8717–E8726. [PubMed: 30150398]
40. Liu J, Liao S, Diop-Frimpong B, Chen W, Goel S, Naxerova K, Ancukiewicz M, Boucher Y, Jain RK, and Xu L. 2012 TGF-β blockade improves the distribution and efficacy of therapeutics in breast carcinoma by normalizing the tumor stroma. Proc Natl Acad Sci U S A 109: 16618–16623. [PubMed: 22996328]
41. Miller MA, and Weissleder R. 2017 Imaging of anticancer drug action in single cells. Nat Rev Cancer 17: 399–414. [PubMed: 28642603]
42. Nakasone ES, Askautrud HA, Kees T, Park JH, Plaks V, Ewald AJ, Fein M, Rasch MG, Tan YX, Qiu J, Park J, Sinha P, Bissell MJ, Frengen E, Werb Z, and Egeblad M. 2012 Imaging tumor-

Author Manuscript

Author Manuscript

Author Manuscript

Author Manuscript

stroma interactions during chemotherapy reveals contributions of the microenvironment to resistance. Cancer Cell 21: 488–503. [PubMed: 22516258]

43. Sparks H, Kondo H, Hooper S, Munro I, Kennedy G, Dunsby C, French P, and Sahai E. 2018 Heterogeneity in tumor chromatin-doxorubicin binding revealed by in vivo fluorescence lifetime imaging confocal endomicroscopy. Nat Commun 9: 2662. [PubMed: 29985394]
44. Thurber GM, Yang KS, Reiner T, Kohler RH, Sorger P, Mitchison T, and Weissleder R. 2013 Single-cell and subcellular pharmacokinetic imaging allows insight into drug action in vivo. Nat Commun 4: 1504. [PubMed: 23422672]
45. Kim E, Yang KS, Kohler RH, Dubach JM, Mikula H, and Weissleder R. 2015 Optimized Near-IR Fluorescent Agents for in Vivo Imaging of Btk Expression. Bioconjug Chem 26: 1513–1518. [PubMed: 26017814]
46. Mikula H, Stapleton S, Kohler RH, Vinegoni C, and Weissleder R. 2017 Design and Development of Fluorescent Vemurafenib Analogs for In Vivo Imaging. Theranostics 7: 1257–1265. [PubMed: 28435463]
47. Miller MA, Kim E, Cuccarese MF, Plotkin AL, Prytyskach M, Kohler RH, Pittet MJ, and Weissleder R. 2017 Near infrared imaging of Mer tyrosine kinase (MERTK) using MERi-SiR reveals tumor associated macrophage uptake in metastatic disease. Chem Commun (Camb) 54: 42–45. [PubMed: 29185561]
48. Turetsky A, Kim E, Kohler RH, Miller MA, and Weissleder R. 2014 Single cell imaging of Bruton's tyrosine kinase using an irreversible inhibitor. Sci Rep 4: 4782. [PubMed: 24759210]
49. Dubach JM, Kim E, Yang K, Cuccarese M, Giedt RJ, Meimetis LG, Vinegoni C, and Weissleder R. 2017 Quantitating drug-target engagement in single cells in vitro and in vivo. Nat Chem Biol 13: 168–173. [PubMed: 27918558]
50. Cabral H, Matsumoto Y, Mizuno K, Chen Q, Murakami M, Kimura M, Terada Y, Kano MR, Miyazono K, Uesaka M, Nishiyama N, and Kataoka K. 2011 Accumulation of sub-100 nm polymeric micelles in poorly permeable tumours depends on size. Nat Nanotechnol 6: 815–823. [PubMed: 22020122]
51. Chauhan VP, Stylianopoulos T, Martin JD, Popović Z, Chen O, Kamoun WS, Bawendi MG, Fukumura D, and Jain RK. 2012 Normalization of tumour blood vessels improves the delivery of nanomedicines in a size-dependent manner. Nat Nanotechnol 7: 383–388. [PubMed: 22484912]
52. Miller MA, Askevold B, Mikula H, Kohler RH, Pirovich D, and Weissleder R. 2017 Nano-palladium is a cellular catalyst for in vivo chemistry. Nat Commun 8: 15906. [PubMed: 28699627]
53. Miller MA, Chandra R, Cuccarese MF, Pfirschke C, Engblom C, Stapleton S, Adhikary U, Kohler RH, Mohan JF, Pittet MJ, and Weissleder R. 2017 Radiation therapy primes tumors for nanotherapeutic delivery via macrophage-mediated vascular bursts. Sci Transl Med 9:
54. Miller MA, Mikula H, Luthria G, Li R, Kronister S, Prytyskach M, Kohler RH, Mitchison T, and Weissleder R. 2018 Modular Nanoparticulate Prodrug Design Enables Efficient Treatment of Solid Tumors Using Bioorthogonal Activation. ACS Nano 12: 12814–12826. [PubMed: 30550257]
55. Harper KL, Sosa MS, Entenberg D, Hosseini H, Cheung JF, Nobre R, Avivar-Valderas A, Nagi C, Girnius N, Davis RJ, Farias EF, Condeelis J, Klein CA, and Aguirre-Ghiso JA. 2016 Mechanism of early dissemination and metastasis in Her2$^+$ mammary cancer. Nature 540: 588–592. [PubMed: 27974798]
56. Benninger RK, and Piston DW. 2013 Two-photon excitation microscopy for the study of living cells and tissues. Curr Protoc Cell Biol Chapter 4: Unit 4.111–24.
57. Chittajallu DR, Florian S, Kohler RH, Iwamoto Y, Orth JD, Weissleder R, Danuser G, and Mitchison TJ. 2015 In vivo cell-cycle profiling in xenograft tumors by quantitative intravital microscopy. Nat Methods 12: 577–585. [PubMed: 25867850]
58. Noy R, and Pollard JW. 2014 Tumor-associated macrophages: from mechanisms to therapy. Immunity 41: 49–61. [PubMed: 25035953]
59. Cilliers C, Menezes B, Nessler I, Linderman J, and Thurber GM. 2018 Improved Tumor Penetration and Single-Cell Targeting of Antibody-Drug Conjugates Increases Anticancer Efficacy and Host Survival. Cancer Res 78: 758–768. [PubMed: 29217763]
60. Canton J 2018 Macropinocytosis: New Insights Into Its Underappreciated Role in Innate Immune Cell Surveillance. Front Immunol 9: 2286. [PubMed: 30333835]

Author Manuscript

Author Manuscript

Author Manuscript

Author Manuscript

61. Müller-Greven G, Carlin CR, Burgett ME, Ahluwalia MS, Lauko A, Nowacki AS, Herting CJ, Qadan MA, Bredel M, Toms SA, Lathia JD, Hambardzumyan D, Sarkaria JN, Hamerlik P, and Gladson CL. 2017 Macropinocytosis of Bevacizumab by Glioblastoma Cells in the Perivascular Niche Affects their Survival. Clin Cancer Res 23: 7059–7071. [PubMed: 28912141]

62. Zhao H, Atkinson J, Gulesserian S, Zeng Z, Nater J, Ou J, Yang P, Morrison K, Coleman J, Malik F, Challita-Eid P, Karki S, Aviña H, Hubert R, Capo L, Snyder J, Moon SJ, Luethy R, Mendelsohn BA, Stover DR, and Doñate F. 2018 Modulation of Macropinocytosis-Mediated Internalization Decreases Ocular Toxicity of Antibody-Drug Conjugates. Cancer Res 78: 2115–2126. [PubMed: 29382707]

63. Dekkers G, Bentlage AEH, Stegmann TC, Howie HL, Lissenberg-Thunnissen S, Zimring J, Rispens T, and Vidarsson G. 2017 Affinity of human IgG subclasses to mouse Fc gamma receptors. MAbs 9: 767–773. [PubMed: 28463043]

64. DiLillo DJ, and Ravetch JV. 2015 Differential Fc-Receptor Engagement Drives an Anti-tumor Vaccinal Effect. Cell 161: 1035–1045. [PubMed: 25976835]

65. Li F, Ulrich M, Jonas M, Stone IJ, Linares G, Zhang X, Westendorf L, Benjamin DR, and Law CL. 2017 Tumor-Associated Macrophages Can Contribute to Antitumor Activity through FcγR-Mediated Processing of Antibody-Drug Conjugates. Mol Cancer Ther 16: 1347–1354. [PubMed: 28341790]

66. Morrissey MA, Williamson AP, Steinbach AM, Roberts EW, Kern N, Headley MB, and Vale RD. 2018 Chimeric antigen receptors that trigger phagocytosis. Elife 7:

67. Mellor JD, Brown MP, Irving HR, Zalcberg JR, and Dobrovic A. 2013 A critical review of the role of Fc gamma receptor polymorphisms in the response to monoclonal antibodies in cancer. J Hematol Oncol 6: 1. [PubMed: 23286345]

Author Manuscript

Author Manuscript

Author Manuscript

Author Manuscript

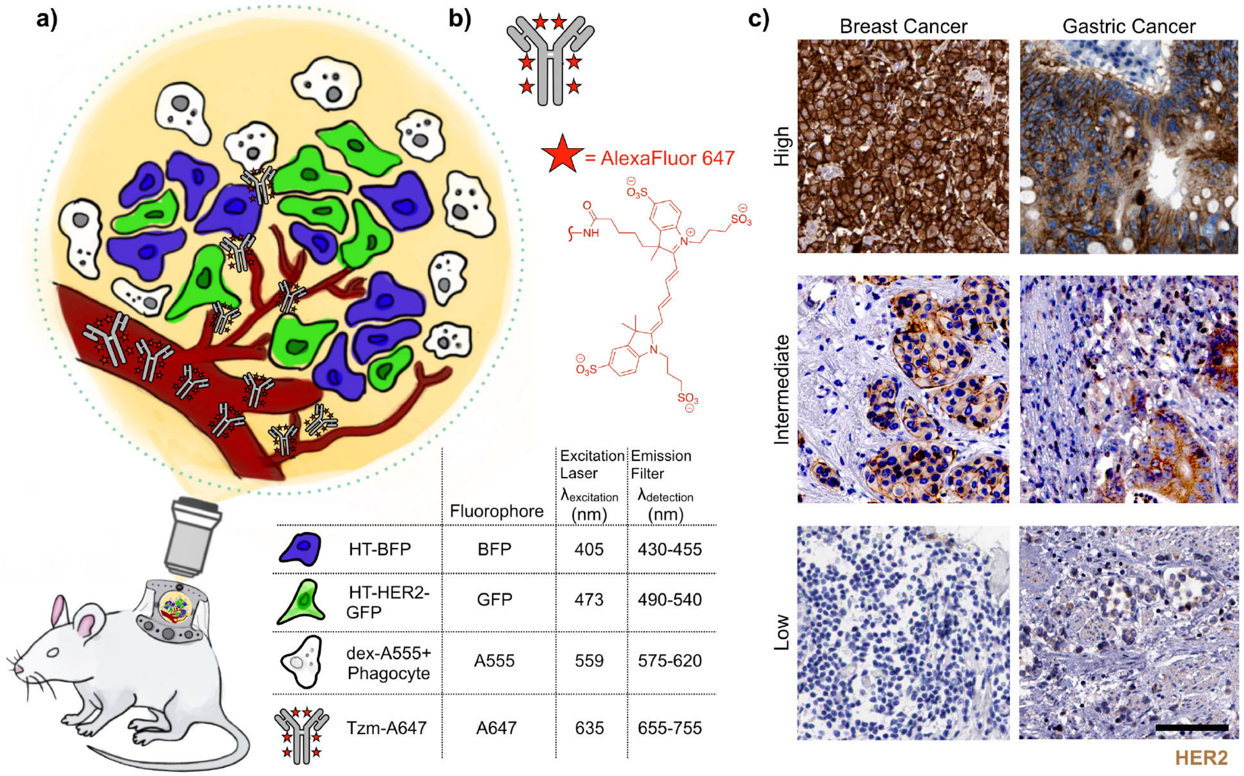

		Fluorophore	Excitation Laser $\lambda_{excitation}$ (nm)	Emission Filter $\lambda_{detection}$ (nm)
	HT-BFP	BFP	405	430-455
	HT-HER2-GFP	GFP	473	490-540
	dex-A555+ Phagocyte	A555	559	575-620
	Tzm-A647	A647	635	655-755

Figure 1. Multichannel intravital microscopy setup.

(a) Schematic of the 4-channel intravital microscopy (IVM) strategy using a xenograft mouse model of cancer. Mosaic tumors are grown subcutaneously in a dorsal window chamber for repeat imaging across hours and days. **(b)**Trastuzumab (Tzm) is labelled with AlexaFluor647 (A647) via NHS-ester coupling. **(c)** From the *Human Protein Atlas* (www.proteinatlas.org, version 18.1), representative immunohistochemistry of HER2 expression in patient biopsies from invasive ductal carcinoma of the breast (left) and gastric cancer (right). Tumors with high HER2 expression (more than 75% of tumor cells showing positive stain, top), intermediate HER2 expression (mosaic expression with 50% of cells showing expression, middle), and low HER2 expression (less than 25% of cells showing expression) are shown. Scale bar=100 μm.

Author Manuscript

Author Manuscript

Author Manuscript

Author Manuscript

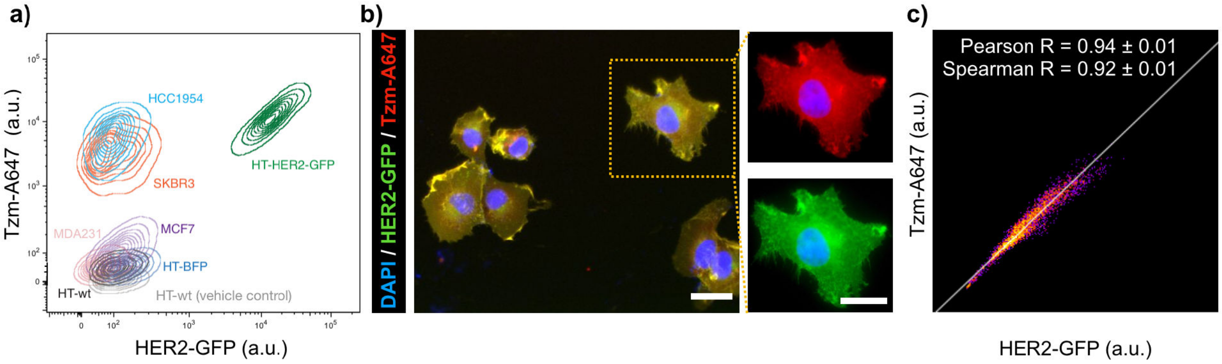

Figure 2. A647 labeled Tzm efficiently and selectively binds HER2 and transgenic HER2-GFP in vitro.

(a) Representative flow cytometry of Tzm-A647 binding to various HER2-high (HCC1954, SKBR3, and HT-HER2-GFP) and HER2-low (MCF7, MDA231, HT-wt, and HT-BFP) cancer cells. HT-wt denotes parental HT1080, and all non-HT cells are breast cancer. Contour lines denote density of single-cell data points. **(b-c)** Representative fluorescent microscopy (**b**, scale bars = 10 μm) and pixel-by-pixel correlation (**c**) of Tzm and HER2-GFP signal intensity showing strong sub-cellar co-localization of Tzm and HER2-GFP fusion protein in HT-HER2-GFP cells (**c**, data are means ± s.e.m.; n=15 cells).

Author Manuscript

Author Manuscript

Author Manuscript

Author Manuscript

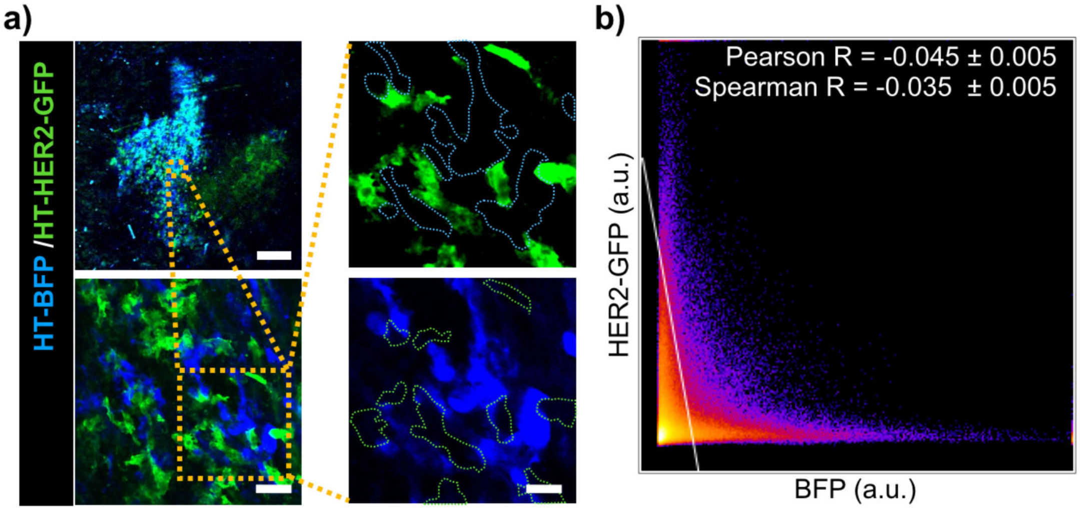

Figure 3. IVM enables segmentation of intermixed HER2− and HER2+ tumor cells in a mosaic xenograft model.

(a-b) HT-BFP and HT-HER2-GFP cells were mixed 1:1, injected into the dorsal window chamber of nu/nu mice, and imaged by IVM upon tumor formation. Representative IVM with single-cell segmentation (**a**) and corresponding pixel-by-pixel analysis of BFP and GFP fluorescence intensities (**b**) show minimal overlap and an ability to distinguish HER2− and HER2+ cells. Data are means ± s.e.m. from all pixels, scale bars: top left panel=0.5 mm; bottom left panel=50 μm; right panels=20 μm.

Author Manuscript

Author Manuscript

Author Manuscript

Author Manuscript

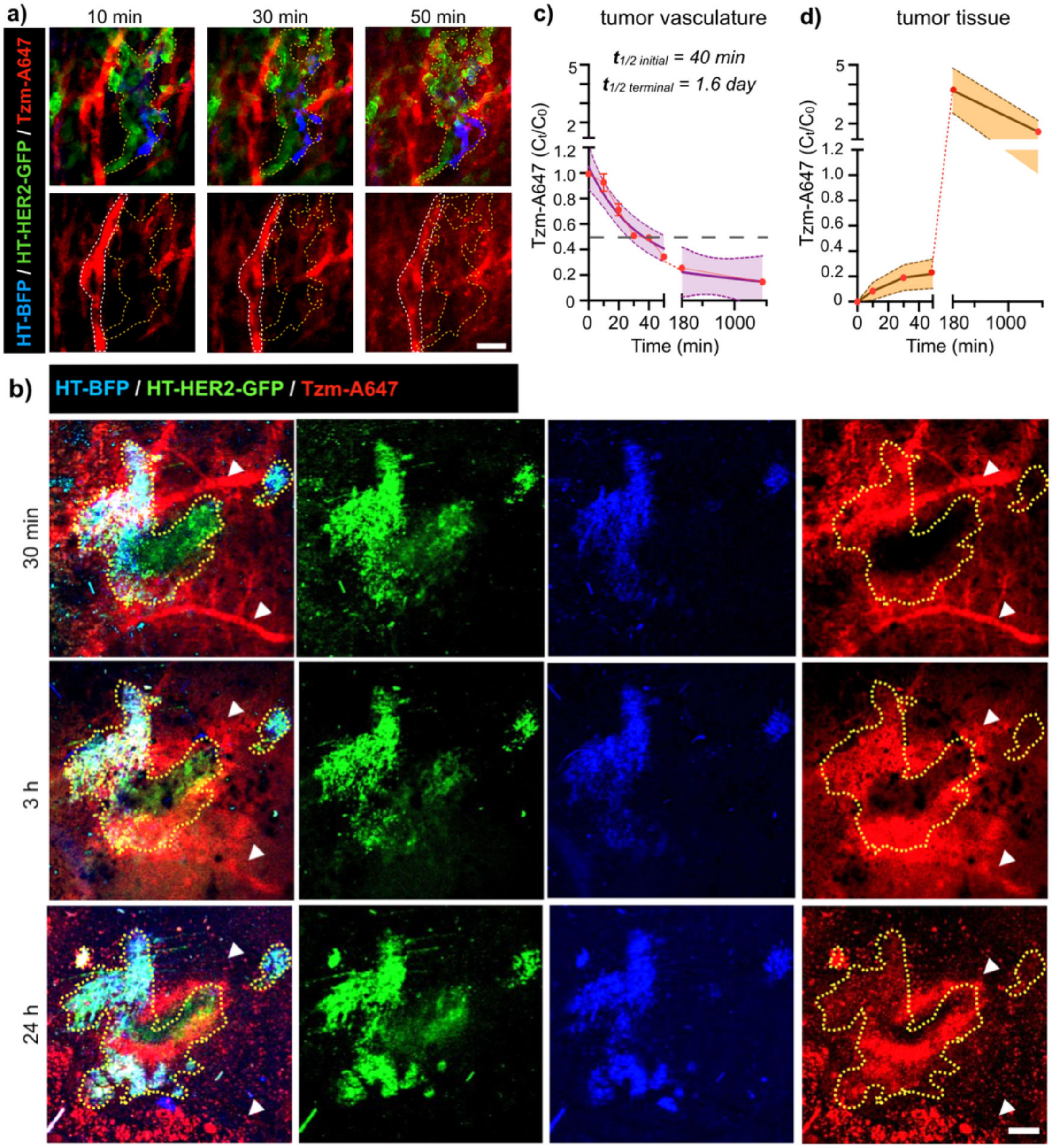

Figure 4. Time-lapse IVM quantifies systemic clearance of Tzm and its accumulation in tumor tissue.

(a-d) Mosaic tumor-bearing nu/nu mice were injected i.v. with Tzm and imaged by IVM at high (**a**, scale bar=50 μm; white outline: blood vessel; yellow outline: tumor cells) and low (**b**, scale bar=500 μm; white arrow: blood vessels; yellow outline: tumor) magnifications. (**c**) IVM quantified Tzm concentration in tumor microvasculature to calculate its systemic blood half-life (data are means ± s.e.m., with purple shading denoting the 95% CI of exponential model fit across n > 45 blood vessel regions from 4 tumors). (**d**) IVM quantified Tzm concentration in extravascular tumor tissue (line and shading denotes means ± s.e.m., n>20 regions from 4 tumors).

Author Manuscript Author Manuscript Author Manuscript Author Manuscript

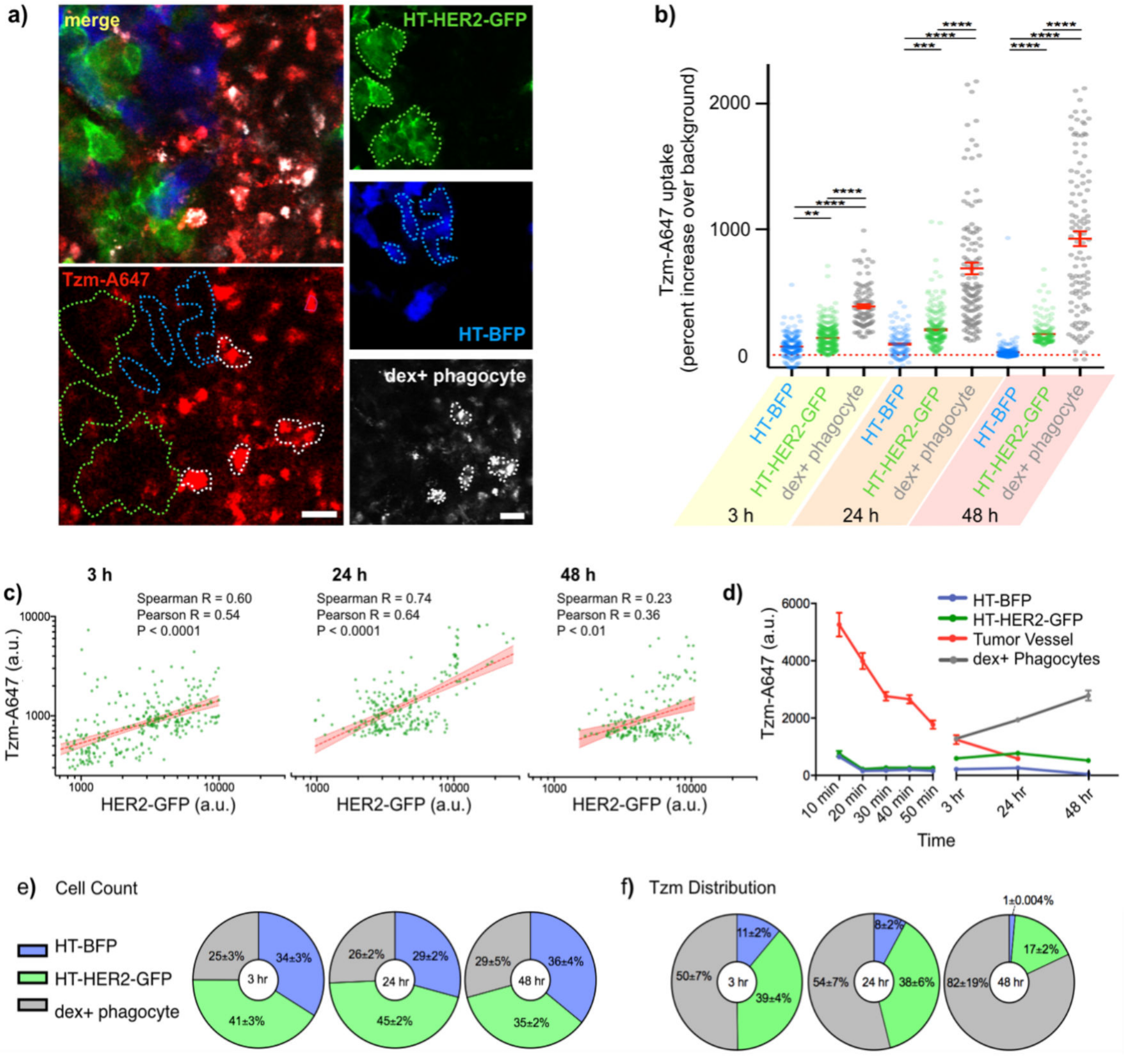

Figure 5. Tzm association with HER2+ tumor cells peaks at 24 h, and shifts to tumor associated phagocytes by 48 h.

(a-b) Representative IVM of the mosaic tumor model (**a**) and single-cell quantification (**b**) reveals Tzm association with HT-BFP, HT-HER2-GFP, and dextran-A555+ phagocytes over time (data are means ± s.e.m from n > 100 cells across 4 tumors, ****: p<0.0001, ***: p<0.001, **: p<0.01, ANOVA test). Scale bars = 20 μm. (**c**) Correlations of HER2-GFP expression and Tzm association were calculated by IVM on a cell-by-cell basis, corresponding to data in *a-b* (Spearman and Pearson correlation R and p-values reported, n > 150 cells). **(d)** Dynamics of Tzm association in each sub-compartment of the mosaic tumor were calculated (mean ± s.e.m. from combined n > 300 cells and n > 15 blood vessel regions across 4 tumors). **(e-f)** The relative prevalence of the 3 imaged cell-types was tabulated from IVM data (**e**), and these data were combined with observed single-cell Tzm levels to calculate overall accumulation of Tzm in each of the three cell-types (**f**). For e-f, data are means ± s.e.m. from n > 70 cells per group across 6 tumor regions.

Author Manuscript Author Manuscript Author Manuscript Author Manuscript

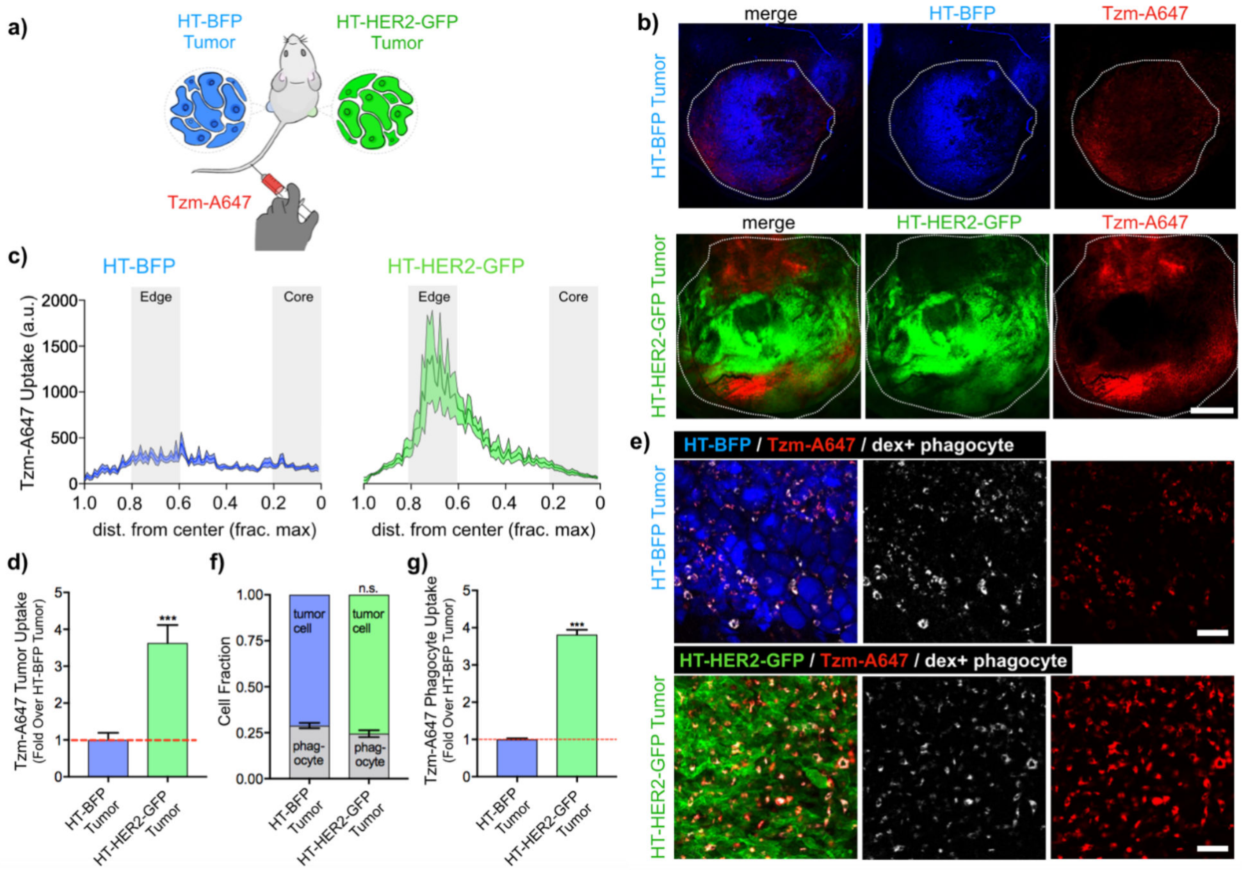

Figure 6. Biodistribution of Tzm in uniformly matched HER2+ or HER2− tumors.

(a) HT-HER2-GFP cells were s.c. injected contralateral to HT-BFP cells in nu/nu subjects. Upon tumor formation, tumors were excised 24 h post-administration with Tzm and dextran-A555. **(b)** Representative confocal microscopy of CUBIC-clarified tumors (white outline denotes tissue edge, scale bar=1 mm). **(c-d)** Radial profiles of Tzm distribution were measured as function of normalized distance from the tumor center (**c**, line and shading denote means ± s.e.m.). The areas under the profile curves were calculated to assess Tzm uptake in the whole tumor (**d**, mean ± s.e.m. across 30 profiles and 6 tumors; ***: $p<0.001$, t-test). **(e-g)** Representative high-magnification confocal microscopy (**e**; scale bars=50 μm) corresponding to *a-b* is quantified as the relative abundance of tumor cells and phagocytes in tumors (**f**), along with phagocyte's association with Tzm (**g**). For *f-g*, data are means ± s.e.m. from n > 250 cells across 6 tumors (***$p<0.001$, n.s.=not significant, t-test).